Robust Sparse Unmixing via Continuous Mixed Norm to Address Mixed Noise

Jincheng Gao, Jiayu Shi, and Fei Zhu, *Member, IEEE*

***Abstract*—Sparse unmixing, a critical task in hyperspectral image interpretation, aims to identify an optimal subset of endmembers from a predefined library and estimate the fractional abundances for each pixel. However, in real-world scenarios, various types of noise significantly degrade the performance of conventional sparse unmixing methods that usually rely on ℓ_2-norm loss function. To address this issue, this letter proposes a robust sparse unmixing method based on the continuous mixed norm (CMN), which exhibits resilience to mixed noise, particularly non-Gaussian impulsive noise. By adopting CMN as the reconstruction loss function, we formulate both the standard sparse unmixing problem and its augmented version with total variation (TV) regularizer for spatially piecewise smoothness. The corresponding algorithms are derived using the alternating direction method of multipliers (ADMM). Experiments on both synthetic and real hyperspectral datasets validate the effectiveness and robustness of the proposed method in handling diverse and mixed noise conditions over comparing methods. The code is available at: https://github.com/JinchengGao/CMNSU**

***Index Terms*—Sparse unmixing, continuous mixing norm (CMN), robust method, alternating direction method of multipliers (ADMM).**

I. Introduction

HYPERSPECTRAL imagery (HSI), which provides abundant spectral information about ground objects under scrutiny, has gained significant attention within the remote sensing community [1]. Due to the limited spatial resolution of imaging sensors, each observed pixel in a hyperspectral image is typically a mixture of several pure materials, known as endmembers. Spectral unmixing seeks to identify these endmembers and estimate their corresponding fractional abundances in each pixel based on a specific mixing model.

While nonlinear models are gaining relevance, the linear mixture model (LMM) remains the most widely studied due to its simplicity and computational efficiency. It represents each pixel as a linear combination of several endmembers, weighted by their corresponding abundances. Unsupervised unmixing methods simultaneously estimate both endmembers and abundances. However, they may extract endmembers that do not correspond to any actual signatures in the spectral library. Sparse unmixing, a semi-supervised approach, addresses this issue by incorporating a predefined endmember library into the unmixing process [1]. Since only a small subset of endmembers contributes to the mixture, the resulting abundances are sparse relative to the full spectral library, which often contains hundreds of signatures.

In this context, sparsity in abundances is enforced through sparsity-promoting regularizers in the loss function. The well-known SUnSAL enforces sparsity using ℓ_1 norm regularization on the abundance [2]. Since only a small subset of endmembers from the library are active during unmixing, row sparsity in the abundance matrix is further enforced using the $\ell_{2,1}$ norm [3] and $\ell_{2,0}$ norm [4]. Additionally, spatial correlation is leveraged to enhance abundance estimation. For example, SUnSAL-TV incorporates total variation (TV) regularization to produce spatially smoother abundance maps [5]. To improve unmixing efficiency, MUA [6] employs multiscale spatial regularization in both segmentation and original image domains. Spatial-spectral information is explored in S^{2}WS [7] through a weighting strategy, while LGSU [8] jointly considers global sparsity and superpixel-guided local sparsity priors. Recently, many unsupervised unmixing networks have explored the spectral-spatial priors on abundance using advanced network architectures such as CNNs and Transformers [9]. Note that the majority of methods rely on the ℓ_2 norm as the reconstruction loss function and perform well for low-noise HSIs affected by Gaussian noise without outliers. However, their unmixing performance deteriorates in the presence of more complex noise scenarios.

In real HSIs, in addition to Gaussian noise, images are often affected by various types of impulsive noise, such as shot noise and dead lines/strips [10], [11], which significantly degrade unmixing performance. To address the non-Gaussian noise and outliers, several alternative reconstruction loss functions have been proposed in sparse unmixing, extending beyond the traditional ℓ_2 norm. Notable examples include the $\ell_{2,1}$ norm [12], [13], correntropy [14], and an adaptive σ-norm loss that combines both ℓ_2 and $\ell_{2,1}$ norms [15]. More recently, the log-cosh loss has been considered effective for handling non-Gaussian noise [16]. In [17], JSTV introduces an additional term to the loss to handle spatially sparse noise, further enhancing robustness against mixed noise.

In theory, impulsive noise can be effectively characterized using stable distributions, particularly the symmetric alpha-stable ($S\alpha S$) distribution [18]. In practice, however, loss functions based on ℓ_p norms are commonly used to model noise using the generalized Gaussian distribution (GGD), defined as $f(x;\alpha,\beta) = \frac{\alpha}{2\beta\Gamma(1/\alpha)} \exp\left(-\left(\frac{|x|}{\beta}\right)^{\alpha}\right)$, where x represents the noise vector, $\Gamma(\cdot)$ is the Gamma function, α is the shape parameter, and β is the scale parameter. Statistically, ℓ_2-norm minimization with least squares corresponds

The work was supported by the National Natural Science Foundation of China under Grant 61701337. *(Corresponding author: Fei Zhu)*

J. Gao and F. Zhu are with the Center for Applied Mathematics, Tianjin University, Tianjin, 300072, China (e-mail: fei.zhu@tju.edu.cn).

J. Shi is with the School of Mathematics, Tianjin University, Tianjin, 300072, China.

to maximum likelihood estimation (MLE) under Gaussian noise assumptions ($\alpha = 2$), while the ℓ_1-norm corresponds to Laplace noise ($\alpha = 1$), demonstrating effectiveness against impulsive noise [19].

However, accurate noise modeling in real HSIs remains challenging due to their complex and mixed characteristics. The impulsive characteristics of non-Gaussian noise cannot be sufficiently captured by single-distribution assumptions, leading to non-trivial norm selection and performance degradation in sparse unmixing. This motivates the use of the continuous mixing norm (CMN), which integrates multiple error norms to address heavy-tailed noise and shows robustness against impulsive noise in adaptive filtering and signal recovery [18], [20]. When handling GGD-modeled noise with unknown α, CMN achieves near-optimal recovery [18]. Its inherent capacity to address heavy-tailed mixed noise correlates with real HSI degradation patterns, establishing CMN as a robust loss function for sparse unmixing.

In this letter, we propose two robust sparse unmixing methods based on the Continuous Mixing Norm (CMN) to address the challenges posed by non-Gaussian impulsive noise, especially in mixed noise scenarios. Unlike previous reconstruction loss functions that rely on fixed or combined norms [12], [13], [15] or complex loss functions [14], [16], our method defines the reconstruction loss by integrating ℓ_p norms by a uniform probability distribution between 1 and 2. This integration allows the model to dynamically adapt to varying noise characteristics, offering enhanced robustness against impulsive noise commonly present in HSIs. To be precise, we first integrate CMN into sparse unmixing, formulating the problem in two versions: the standard form (CMNSU) and a TV-regularized version (CMNSU-TV) to enforce spatial consistency in the abundance maps. The corresponding optimization problems are solved using the nonconvex ADMM framework, with closed-form update rules derived for each variable. Experiments on both synthetic and real images validate the effectiveness of the proposed method, showcasing its robustness in handling mixed noise conditions.

The letter is organized as follows. Section II presents the proposed robust sparse unmixing method using CMN. Section III presents the experimental results. Finally, Section IV concludes the letter.

II. Proposed Robust Sparse Unmixing using Continuous Mixed Norm

Let $Y \in \mathbb{R}^{L\times N}$ represent an observed hyperspectral image composed of N pixels across L spectral bands, where each column of Y corresponds to a pixel. In the context of sparse unmixing, we assume that endmember matrix E, provided a priori, is a spectral library containing R spectral signatures. Since only a few of the signatures in E are likely to contribute to the observed spectra for each pixel, the abundance matrix X is typically sparse.

Rather than relying on fixed-norm loss functions, *e.g.*, the ℓ_2 norm [5] or $\ell_{2,1}$ norm [12], we propose using CMN, integrating p between 1 and 2, characterized by a uniform distribution $\lambda(p) = 1$, to define the reconstruction loss function in sparse unmixing. This leads to the following optimization problem:

$$\min_{X\geq 0} \int_1^2 \|Y - EX\|_p^p \, dp + \mu\|X\|_1, \tag{1}$$

where $\int_1^2 \|X\|_p^p \, dp \triangleq \sum_{i,j} \int_1^2 |X_{i,j}|^p \, dp$ provides a robust reconstruction function and the second term enforces sparsity in the abundance matrix. Additionally, we enforce the abundance nonnegativity constraint to ensure physical interpretability.

In parallel to SUnSAL-TV [5], we further consider a TV-regularized version to promote spatially piecewise smoothness in the abundance, yielding the following optimization problem:

$$\min_{X\geq 0} \int_1^2 \|Y - EX\|_p^p \, dp + \mu\|X\|_1 + \eta\mathrm{TV}(X), \tag{2}$$

where $\mathrm{TV}(\cdot)$ denotes the total-variation operator.

The use of CMN as the reconstruction loss function offers advantages by enhancing robustness of unmixing while avoiding assumptions about the noise distribution, in contrast to fixed ℓ_p norms. By employing a uniform distribution of p values from 1 to 2, this mixed norm flexibly adapts to a variety of noise characteristics. Notably, in ℓ_p norm problems with $p \in (0, 2]$, the value of p reflects the impulsive nature of the noise, with smaller p values suited highly impulsive noise. However, as p approaches 0, the optimization problem becomes increasingly nonconvex and nonsmooth, complicating the minimization process [21]. As a result, we consider CMN with $p \in (1, 2]$ as a practical balance between robustness and computational feasibility.

A. ADMM for CMNSU

We apply ADMM [22] to solve the optimization problem in (1), and the resulting CMNSU algorithm is summarized in Algorithm (1). The main innovation is using ADMM to solve the non-convex problem derived from CMN. A matrix-based surrogate function generalizes the original vector-based CMN [18], enabling more efficient optimization within the ADMM framework. Despite the complexity of CMN, each subproblem has a closed-form solution, ensuring computational efficiency for tackling real HSIs.

By introducing auxiliary variables V_1,V_2,V_3,V_4, the problem (1) is reformulated as

$$\begin{aligned}\min_{X,\{V_i\}_{i=1}^4} &\int_1^2 \|V_1\|_p^p \, dp + \mu\|V_3\|_1 + \iota_+(V_4) \\ &s.t.\ V_1 = EV_2 - Y, V_2 = X, V_3 = X, V_4 = X,\end{aligned} \tag{3}$$

where $\iota_+(\cdot)$ is the indicator function for the nonnegative orthant $\mathbb{R}^+$. The augmented Lagrangian function is

$$\begin{aligned}\mathcal{L}(X, V_1, V_2, V_3, V_4) = &\int_1^2 \|V_1\|_p^p \, dp + \mu\|V_3\|_1 + \iota_+(V_4) + \\ &\frac{\gamma}{2}\Big(\|V_1 - EV_2 + Y + \Lambda_1/\gamma\|_F^2 + \sum_{i=2}^4 \|V_i - X + \Lambda_i/\gamma\|_F^2\Big)\end{aligned} \tag{4}$$

where $\gamma > 0$ and $\{\Lambda_i/\gamma\}_{i=1}^4$ are Lagrange multipliers.

The V_1-problem is

$$\min_{V_1} \quad \mathcal{C}(V_1) + \frac{\gamma}{2}\Big(\|V_1 - EV_2 + Y + \frac{\Lambda_1}{\gamma}\|_F^2\Big), \tag{5}$$

where $\mathcal{C}(X) \triangleq \int_1^2 \|X\|_p^p \, dp$. To solve (5), we need to find a surrogate function $\mathcal{C}_S(X, X^{'})$ for $\mathcal{C}(X)$, *i.e.*, $\mathcal{C}_S(X, X) = \mathcal{C}(X)$ and $\mathcal{C}_S(X, X^{'}) > \mathcal{C}(X)$, for $X \neq X'$, by following the similar strategy presented in [18].

Lemma 1. *For any $0 < p \leq q$ and x', $|x|^p$ has a surrogate function given by $(|x|^q \left(\frac{p}{q}|x'|^{p-q}\right) + \left(1 - \frac{p}{q}\right)|x'|^p$ [18].*

Using Lemma (1), we have

$$\begin{aligned}
\mathcal{C}(X) &= \sum_{i,j} \int_1^2 |X_{ij}|^p \, dp \\
&\leqslant \sum_{i,j} \int_1^2 |X_{ij}|^q \left(\frac{p}{q}\left|X'_{ij}\right|^{p-q}\right) + \left(1 - \frac{p}{q}\right)\left|X'_{ij}\right|^p \, dp \\
&= \sum_{i,j} |X_{ij}|^q \, \phi_{1,2}^{(q)}(X'_{ij}) + \sum_{i,j} \psi_{1,2}^{(q)}(X'_{ij}) = \mathcal{C}_S(X, X').
\end{aligned} \tag{6}$$

Letting $q = 2$, $\phi_{1,2}^{(q)}(X'_{ij})$ is computed by integration as

$$\phi_{1,2}^{(2)}\left(X'_{ij}\right) = \frac{|X'_{ij}|^2(2\log|X'_{ij}| - 1) - |X'_{ij}|(\log|X'_{ij}| - 1)}{2|X'_{ij}|^2 \log^2|X'_{ij}|}. \tag{7}$$

By combining (6) and (7), we define the surrogate function for $\mathcal{C}(V_1)$ as $\mathcal{C}_S(V_1, {V_1}^k) = \sum_{i,j} \phi_{1,2}^{(2)}({V_1}_{,ij}^{\,k}) V_{1,ij}^2$, where k denotes the iteration number. Consequently, the V_1-problem in (5) transforms into a quadratic problem, which admits a closed-form solution

$$V_1^{k+1} = \Big(\gamma(EV_2^k - Y) + \Lambda_1^k\Big) / \Big(2\phi_{1,2}^{(2)}({V_1}_{,ij}^{\,k}) + \gamma\Big). \tag{8}$$

The remaining sub-problems associated with the Lagrangian function (4) can be efficiently solved using either closed-form solutions or the soft-thresholding operator.

The V_2-problem is quadratic, yielding the following closed-form solution

$$V_2^{k+1} = (E^T E + I)^{-1}\left(X^k + E^\top V_1^k + E^\top \frac{\Lambda_1^k}{\gamma} - \frac{\Lambda_2^k}{\gamma} + E^\top Y\right). \tag{9}$$

The V_3-problem combines a quadratic term with ℓ_1 regularization, which is addressed by the soft-thresholding operator

$$V_3^{k+1} = \text{soft}_{\mu/\gamma}\left(X^k - \Lambda_1^k/\gamma\right), \tag{10}$$

where $\text{soft}_{\mu/\gamma} = \text{sign}(\mu)\max\{|\mu| - \gamma, 0\}$ represents the element-wise application of the soft-thresholding operator.

The sub-problem for V_4 is formulated as

$$\min_{V_4} \frac{\gamma}{2}\|V_4 - X + \Lambda_4/\gamma\|_F^2 + \iota_+(V_4),$$

with the first-order optimality condition $\gamma(V_4 - X + \Lambda_4/\gamma) = 0$. Considering the non-negativity constraint, the solution is further projected onto the non-negative orthant, resulting in

$$V_4^{(k+1)} = \max\left(X - \Lambda_4/\gamma, 0\right). \tag{11}$$

The X-problem is quadratic, admiting a closed-form solution given by

$$X^{k+1} = (V_2^k + V_3^k + V_4^k)/3 + (\Lambda_2^k + \Lambda_3^k + \Lambda_4^k)/3\gamma. \tag{12}$$

Algorithm 1 Pseudocode for CMNSU algorithm.

Input: Y, E and parameters $\mu, \gamma > 0$.
Output: $\hat{X}$
Initialize $X^0, \{V_i^0, \Lambda_i^0\}_{i=1}^4, k = 0$.
while *stopping criterion is not satisfied* **do**
  Update $\{V_i^{k+1}\}_{i=1}^4$ and X^{k+1} by (8)-(12)
  $\Lambda_1^{k+1} = \Lambda_1^k + \gamma(V_1^k - EV_2^k + Y)$
  $\Lambda_i^{k+1} = \Lambda_i^k + \gamma(V_i^k - X^k)$, $i = 2, 3, 4$
  $k = k + 1$
end while
return $\hat{X} = X^{k+1}$

Algorithm 2 Pseudocode for CMNSU-TV algorithm.

Input: Y, E and parameters $\mu, \eta, \gamma > 0$.
Output: $\hat{X}$
Initialize $X^0, \{V_i^0, \Lambda_i^0\}_{i=1}^5, k = 0$.
while *stopping criterion is not satisfied* **do**
  Update $\{V_i^{k+1}\}_{i=1}^4$ and X^{k+1} by (8)-(11) and (13)
  Update V_5^{k+1} by $V_5^{k+1} = \nabla X^{k+1}$
  $\Lambda_1^{k+1} = \Lambda_1^k + \gamma(V_1^k - EV_2^k + Y)$
  $\Lambda_i^{k+1} = \Lambda_i^k + \gamma(V_i^k - X^k)$, $i = 2, 3, 4$
  $\Lambda_5^{(k+1)} = \Lambda_5^{(k)} + \gamma(V_5^k - \nabla X^k)$
  $k = k + 1$
end while
return $\hat{X} = X^{k+1}$

B. ADMM for CMNSU-TV

We apply the ADMM to solve the problem in (2), resulting in Algorithm (2). To this end, the optimization problem is reformulated as

$$\begin{aligned}
&\min_{X, \{V_i\}_{i=1}^5} \int_1^2 \|V_1\|_p^p \, dp + \mu\|V_3\|_1 + \iota_+(V_4) + \eta\text{TV}(V5) \\
&s.t.\ V_1 = EV_2 - Y, V_2 = X, V_3 = X, V_4 = X, V_5 = \nabla X.
\end{aligned}$$

In particular, the X-problem is expressed as

$$\arg\min_X \sum_{i=2}^4 \|V_i - X + \Lambda_i/\gamma\|_F^2 + \|V_5 - \nabla X + \Lambda_5/\gamma\|_F^2,$$

which is solved using Fast Fourier Transform (FFT), denoted as $\mathcal{F}$, by transforming the problem into the frequency domain

$$X^{(k+1)} = \mathcal{F}^{-1}\Big(\frac{\mathcal{F}\left(\sum_{i=2}^4 (V_i + \Lambda_i/\gamma) + \nabla V_5 + \nabla\Lambda_5/\gamma\right)}{3 + \mathcal{F}(\Delta)}\Big). \tag{13}$$

III. Experiments

The proposed CMNSU and CMNSU-TV algorithms are evaluated on two synthetic datasets, DC1 and DC2, as well as a real Cuprite image. Six state-of-the-art sparse unmixing methods are selected for comparision, including SUnSAL [2], SUnSAL-TV [5], MUA SLIC [6], LGSU [8], JSTV [17], and S^{2}WS [7]. We employ the signal-to-reconstruction error (SRE) as a metric to evaluate the unmixing performance, which is defined as $\text{SRE} = 10\log_{10}\left[\frac{\mathbb{E}(\|X\|_F^2)}{\mathbb{E}(\|X - \hat{X}\|_F^2)}\right]$, where X and $\hat{X}$ represent the ground truth (GT) and estimated abundance, respectively, and $\mathbb{E}(\cdot)$denotes the expectation function.

To find the optimal parameters for the competing methods, for each experiment, the parameters are tuned within

the range $[1e{-}5, 1e5]$, as specified in their respective papers. For CMNSU, we tune μ and η from the set $\{1e{-}5, 5e{-}5, \ldots, 1e2\}$; for CMNSU-TV, we tune μ and η within the same set and λ within $\{1e{-}2, 5e{-}2, \ldots, 1e2\}$. The parameters that yield the highest SRE values are used for comparison.

A. Simulation Results on DC1 and DC2

For the endmember library E_1 used in the experiments on synthetic datasets, we employ a collection of 240 materials from the USGS spectral library, ensuring that the angle between any two endmembers exceeds $4.44°$.

DC1 contains 5 endmembers selected from E_1 and consists of 75×75 pixels. Its abundance maps are generated by square regions uniformly distributed across a background in five rows. DC2 includes 9 endmembers chosen from E_1 and consists of 100×100 pixels, with abundance maps sampled from a Dirichlet distribution, centered around a Gaussian random field [6]. Finally, both datasets were corrupted by three complex mixed-noise scenarios to simulate real hyperspectral image conditions, as outlined in [11].

- **Noise Case 1** (Non-i.i.d. Gaussian Noise): Each band is corrupted by Gaussian noise, with the signal-to-noise ratio (SNR) randomly sampled between 25 dB and 35 dB for each band.
- **Noise Case 2** (Gaussian+Impulse Noise): Building upon Case 1, an additional 5% impulse noise is introduced to each band, further corrupting the data.
- **Noise Case 3** (Gaussian+Impulse+Deadlines): Extending Case 2, 30% of the bands are randomly selected and corrupted by deadlines, as described in [10].

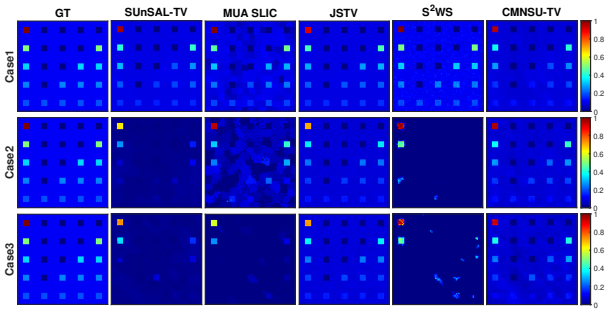

Fig. 1. Abundance map of End #1, estimated by different unmixing methods on DC1. (Top to Bottom): Noise case 1, Noise case 2, and Noise case 3.

Table I presents the unmixing performance measured by SRE for DC1 and DC2. Table I presents the unmixing performance measured by SRE for DC1 and DC2. In Noise case 1, which involves non-i.i.d Gaussian noise, MUA and S^{2}WS demonstrated superior unmixing performance due to their advanced spatial-spectral regularization techniques. CMNSU achieved comparable SRE to SUnSAL, while CMNSU-TV underperformed relative to SUnSAL-TV. This suggests that CMN-based sparse unmixing methods can match the performance of the ℓ_2-based reconstruction loss function in Gaussian noise scenarios. In Noise cases 2 and 3, which involve more impulsive and heavy-tailed noise types, the performance of the competing methods significantly declined. In contrast, the proposed CMNSU outperformed SUnSAL, and CMNSU-TV achieved the highest SRE across both datasets. These results highlight the robustness of the proposed method in handling heavy-tailed, impulsive mixed noise.

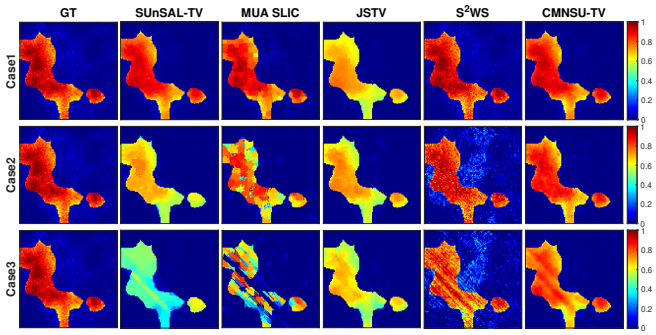

Fig. 2. Abundance map of End #1, estimated by different unmixing methods on DC2. (Top to Bottom): Noise case 1, Noise case 2, and Noise case 3.

Figures 1 and 2 visualize the abundance maps of a single endmember from both datasets, obtained using the GT, SUnSAL-TV, MUA-SLIC, JSTV, S^{2}WS, and the proposed CMNSU-TV, under each of the three noise cases. Visually, the abundance maps by CMNSU-TV are least affected by noise and most closely align with the GT. This is particularly evident in Noise Cases 2 and 3 on DC2, where CMNSU-TV preserves the spatial structure despite the heavy-tailed impulsive noise.

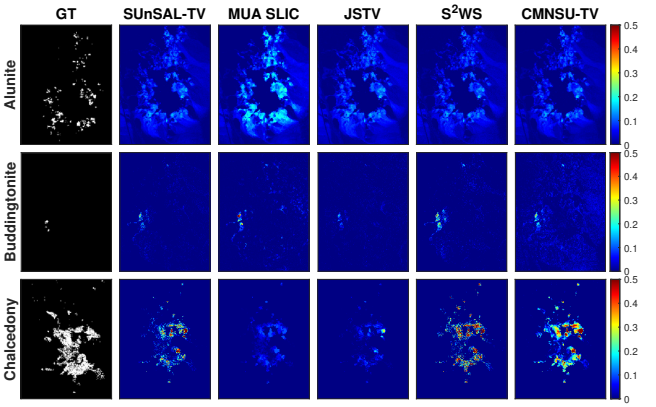

Fig. 3. Abundance maps of Alunite, Buddingtonite, and Chalcedony, estimated by the different unmixing methods on Cuprite.

B. Experimental Results on Cuprite

We evaluate the performance of the proposed method on the real Cuprite dataset, which consists of 250×190 pixels captured by the AVIRIS sensor. For analysis, 187 out of 224 spectral bands are retained. The endmember library E_2 used in this experiment is the complete USGS spectral library, containing 498 endmembers, with the same bands retained as those in the dataset. The parameters for CMNSU-TV are set as $\mu = 1e{-}1$, $\eta = 1e{-}3$, and $\gamma = 1e-1$.

Figure 3 compares the abundance maps for Alunite, Buddingtonite, and Chalcedony, where the GT is the mineral distribution map generated by Tricorder 3.3 [16]. While similar abundance maps are produced, the CMNSU-TV exhibits better alignment with the GT compared to the competing methods,

TABLE I
COMPARISON OF SREs (DB) ON DC1 AND DC2

		SUnSAL	SUnSAL-TV	MUA	JSTV	LGSU	S^2WS	CMNSU	CMNSU-TV
DC1	1	7.63	14.37	15.70	13.09	14.43	**17.63**	9.24	13.85
	2	2.38	8.22	8.29	11.43	3.84	4.75	7.65	**12.64**
	3	1.88	7.00	6.19	11.44	2.99	3.78	7.20	**11.60**
DC2	1	9.96	17.13	17.36	7.17	19.94	**21.32**	9.65	14.60
	2	2.79	6.97	8.44	7.42	3.73	4.11	7.56	**12.98**
	3	2.25	4.64	4.45	6.27	3.60	3.87	6.83	**12.26**

TABLE II
COMPARISON OF RUNNING TIME (IN SECONDS) ON CUPRITE.

SUNSAL	Sunsal-TV	MUA	JSTV	LGSU	S^2WS	CMNSU	CMNSU-TV
69	494	12	1229	400	763	231	908

particularly in preserving spatial structure and effectively handling noise, especially for Chalcedony. TABLE II reports the running time of the comparing methods. The longer running times of CMNSU and CMNSU-TV are attributed to the complexity of the CMN-based reconstruction loss function. However, by utilizing ADMM and closed-form solutions, both methods maintain a comparable computational efficiency feasible for practical applications.

IV. CONCLUSION

In this letter, we propose utilizing the continuous mixing norm as the reconstruction loss function for robust sparse unmixing in hyperspectral images, effectively addressing the challenges posed by complex mixed noise types, particularly non-Gaussian impulsive noise. We consider both the standard sparse unmixing problem and a TV-regularized version, solving the resulting optimization problems using the ADMM. Experiments on both synthetic and real images demonstrate the robustness of our approach in managing various noise scenarios. Future work will extend the continuous mixing norm as a robust reconstruction loss function to nonlinear unmixing models [23], [24], as well as to other restoration tasks in HSIs, such as denoising and reconstruction.

REFERENCES

[1] J. Peng, W. Sun, H.-C. Li, W. Li, X. Meng, C. Ge, and Q. Du, "Low-rank and sparse representation for hyperspectral image processing: A review," *IEEE Geosci. Remote Sens. Mag.*, vol. 10, no. 1, pp. 10–43, 2022.

[2] J. M. Bioucas-Dias and M. A. Figueiredo, "Alternating direction algorithms for constrained sparse regression: Application to hyperspectral unmixing," in *2010 2nd WHISPERS*. IEEE, 2010, pp. 1–4.

[3] M.-D. Iordache, J. M. Bioucas-Dias, and A. Plaza, "Collaborative sparse regression for hyperspectral unmixing," *IEEE Trans. Geosci. Remote Sens.*, vol. 52, no. 1, pp. 341–354, 2014.

[4] J.-J. Wang, T.-Z. Huang, J. Huang, H.-X. Dou, L.-J. Deng, and X.-L. Zhao, "Row-sparsity spectral unmixing via total variation," *IEEE J. Sel. Top. Appl. Earth Obs. Remote Sens.*, vol. 12, no. 12, pp. 5009–5022, 2019.

[5] M.-D. Iordache, J. M. Bioucas-Dias, and A. Plaza, "Total variation spatial regularization for sparse hyperspectral unmixing," *IEEE Trans. Geosci. Remote Sens.*, vol. 50, no. 11, pp. 4484–4502, Nov 2012.

[6] R. A. Borsoi, T. Imbiriba, J. C. M. Bermudez, and C. Richard, "A fast multiscale spatial regularization for sparse hyperspectral unmixing," *IEEE Geosci. Remote Sens. Lett.*, vol. 16, no. 4, pp. 598–602, 2018.

[7] S. Zhang, J. Li, H.-C. Li, C. Deng, and A. Plaza, "Spectral-spatial weighted sparse regression for hyperspectral image unmixing," *IEEE Trans. Geosci. Remote Sens.*, vol. 56, no. 6, pp. 3265–3276, 2018.

[8] X. Shen, H. Liu, X. Zhang, K. Qin, and X. Zhou, "Superpixel-guided local sparsity prior for hyperspectral sparse regression unmixing," *IEEE Geosci. Remote Sens. Lett.*, vol. 19, pp. 1–5, 2022.

[9] J. Chen, M. Zhao, X. Wang, C. Richard, and S. Rahardja, "Integration of physics-based and data-driven models for hyperspectral image unmixing: A summary of current methods," *IEEE Signal Process. Mag.*, vol. 40, no. 2, pp. 61–74, 2023.

[10] L. Zhuang and M. K. Ng, "Fasthymix: Fast and parameter-free hyperspectral image mixed noise removal," *IEEE Trans. Neural Netw. Learn. Syst.*, vol. 34, no. 8, pp. 4702–4716, 2021.

[11] S. Xu, X. Cao, J. Peng, Q. Ke, C. Ma, and D. Meng, "Hyperspectral image denoising by asymmetric noise modeling," *IEEE Trans. Geosci. Remote Sens.*, vol. 60, pp. 1–14, 2022.

[12] M. Yong, L. Chang, X. Mei, C. Liu, and J. Ma, "Robust sparse hyperspectral unmixing with l_{21} norm," *IEEE Trans. Geosci. Remote Sens.*, vol. 55, no. 3, pp. 1227–1239, 2017.

[13] J. Li, Y. Li, R. Song, S. Mei, and Q. Du, "Local spectral similarity preserving regularized robust sparse hyperspectral unmixing," *IEEE Trans. Geosci. Remote Sens.*, vol. 57, no. 10, pp. 7756–7769, 2019.

[14] F. Zhu, A. Halimi, P. Honeine, B. Chen, and N. Zheng, "Correntropy maximization via admm: Application to robust hyperspectral unmixing," *IEEE Trans. Geosci. Remote Sens.*, vol. 55, no. 9, pp. 4944–4955, 2017.

[15] X. Zhang, Y. Yuan, and X. Li, "Sparse unmixing based on adaptive loss minimization," *IEEE Trans. Geosci. Remote Sens.*, vol. 60, pp. 1–14, 2022.

[16] Y. Y. Chan, X.-P. Li, J. Mai, C.-S. Leung, and H. Cheung So, "Sparse unmixing in the presence of mixed noise using l_0-norm constraint and log-cosh loss," *IEEE Trans. Geosci. Remote Sens.*, vol. 62, pp. 1–19, 2024.

[17] H. K. Aggarwal and A. Majumdar, "Hyperspectral unmixing in the presence of mixed noise using joint-sparsity and total variation," *IEEE J. Sel. Top. Appl. Earth Obs. Remote Sens.*, vol. 9, no. 9, pp. 4257–4266, 2016.

[18] A. Javaheri, H. Zayyani, M. A. Figueiredo, and F. Marvasti, "Robust sparse recovery in impulsive noise via continuous mixed norm," *IEEE Signal Process. Lett.*, vol. 25, no. 8, pp. 1146–1150, 2018.

[19] D. Kong, C. Ding, and H. Huang, "Robust nonnegative matrix factorization using l21-norm," in *Proceedings of the 20th ACM International Conference on Information and Knowledge Management (CIKM)*. Association for Computing Machinery, 2011, pp. 673–682.

[20] H. Zayyani, "Continuous mixed p-norm adaptive algorithm for system identification," *IEEE Signal Process. Lett.*, vol. 21, no. 9, pp. 1108–1110, 2014.

[21] W.-J. Zeng and H. C. So, "Outlier-robust matrix completion via ℓ_p -minimization," *IEEE Trans. Signal Process.*, vol. 66, no. 5, pp. 1125–1140, 2018.

[22] S. Boyd, N. Parikh, E. Chu, B. Peleato, and J. Eckstein, "Distributed optimization and statistical learning via the alternating direction method of multipliers," *Foundations and Trends in Machine Learning*, vol. 3, no. 1, pp. 1–122, 2011.

[23] T. Fang, F. Zhu, and J. Chen, "Hyperspectral unmixing based on multilinear mixing model using convolutional autoencoders," *IEEE Trans. Geosci. Remote Sens.*, vol. 62, pp. 1–16, 2024.

[24] M. Li, B. Yang, and B. Wang, "Emlm-net: An extended multilinear mixing model-inspired dual-stream network for unsupervised nonlinear hyperspectral unmixing," *IEEE Trans. Geosci. Remote Sens.*, vol. 62, pp. 1–16, 2024.